Synergistic Utilization of Spaceborne SAR Observations for Monitoring the Baltic Sea Flow Through the Danish Straits

AGU ADVANCING EARTH AND SPACE SCIENCES

Earth and Space Science

RESEARCH ARTICLE
10.1029/2024EA003794

Synergistic Utilization of Spaceborne SAR Observations for Monitoring the Baltic Sea Flow Through the Danish Straits

Anis Elyouncha[1,2], **Göran Broström**[1], **and Harald Johnsen**[3]

[1]University of Gothenburg, Gothenburg, Sweden, [2]Chalmers University of Technology, Gothenburg, Sweden, [3]Norwegian Research Centre (NORCE), Tromsø, Norway

Key Points:

- The dominant processes that govern the sea surface circulation in the Danish strait Fehmarn Belt exhibit time scales larger than 2 days
- To properly sample Baltic Sea time scales, data from three satellites are combined to achieve an average revisit time of 1.2 days
- SAR is capable of monitoring the synoptic scale circulation of the Baltic Sea with adequate temporal resolution and high accuracy

Correspondence to:

A. Elyouncha,
anis.elyouncha@gu.se

Citation:

Elyouncha, A., Broström, G., & Johnsen, H. (2024). Synergistic utilization of spaceborne SAR observations for monitoring the Baltic Sea flow through the Danish straits. *Earth and Space Science*, *11*, e2024EA003794. https://doi.org/10.1029/2024EA003794

Received 31 MAY 2024
Accepted 8 SEP 2024

Author Contributions:

Conceptualization: Anis Elyouncha
Data curation: Anis Elyouncha, Harald Johnsen
Formal analysis: Anis Elyouncha, Göran Broström
Funding acquisition: Anis Elyouncha
Investigation: Anis Elyouncha, Göran Broström
Methodology: Anis Elyouncha
Project administration: Anis Elyouncha
Resources: Anis Elyouncha, Harald Johnsen
Software: Anis Elyouncha
Supervision: Anis Elyouncha, Göran Broström, Harald Johnsen
Validation: Anis Elyouncha
Visualization: Anis Elyouncha
Writing – original draft: Anis Elyouncha
Writing – review & editing: Anis Elyouncha, Göran Broström, Harald Johnsen

Abstract Synthetic aperture radar (SAR) has emerged as a key instrument in oceanography due to its high spatial resolution and sensitivity to ocean surface dynamics. The main limitation of a single spaceborne SAR is the long repeat cycle (e.g., 12 days for Sentinel-1), which hinders its capability to monitor the temporal evolution of oceanic processes. The principal objective of this study is to demonstrate the potential of spaceborne SAR to monitor the temporal variation of ocean surface circulation. This is assessed using the Baltic Sea flow through the Danish strait Fehmarn Belt as a case study. In order to overcome the temporal sampling limitation, data from three satellites are combined, namely Sentinel-1A, Sentinel-1B and TanDEM-X. The average revisit time achieved by combining the three satellites is 1.2 days. Two months of opportunistic SAR data (June and July 2020) covering the Fehmarn Belt are used. The radial surface current derived from SAR is compared to ocean model and in situ data. It is shown that the dominant processes that govern the circulation in the Fehmarn Belt exhibit time scales larger than 2 days. Subsequently, it is demonstrated that SAR effectively captures the synoptic-scale features (time scales larger than 2 days) of the Baltic Sea circulation, thereby enabling monitoring the temporal variations of flow dynamics. Comparison of the SAR-derived radial surface current against in situ measurements yields comparable bias ($\leq$0.08 m/s) and correlation coefficient ($R \approx 0.75$) but lower standard deviations and rms errors (0.15 m/s) than those exhibited by the ocean model (0.31 m/s).

Plain Language Summary Synthetic aperture radar (SAR) provides high resolution images of the ocean surface from space. These images contain information on the roughness of the ocean surface, which is related to wind speed and wave height, and information on the motion of the surface which is related to the wave propagation and surface currents. The ocean surface is dynamic. However, it changes rapidly in some regions and slowly in other regions. This depends on the time scale of the forces driving the circulation in that region. The main limitation of satellites for ocean observation is that they do not pass often over the same area. In this study, we investigate the time scale of the dominant driving processes like sea level and wind in the Danish straits area. This area contains important channels for water exchange between the Baltic Sea and the North Sea. Our investigation reveals that the dominant time scale governing forcing processes in this region exceeds 2 days. Furthermore, through the synergistic utilization of data from three satellite platforms, we demonstrate the capability to effectively resolve the surface flow dynamics of the Baltic Sea with a high degree of precision.

1. Introduction

The water exchange between the Baltic Sea and the open ocean through the Danish straits is very important for hydrographic conditions in the Baltic Sea. The inflows of saline water are rich in oxygen and impact the chemistry and biology of the sub-basins water (Feistel et al., 2008). The two straits, Belt Sea strait and Öresund strait, connecting Baltic Sea to North Sea, are both narrow and shallow. The inflows through these straits to the Baltic Sea has an important influence on the oxygen development in the deep water in the southern and central basins of the Baltic Proper (Gustafsson, 1997). In addition, the Baltic Sea's various straits and sills provide a natural laboratory to understand the mechanisms governing water exchange and mixing, which is of considerable interest to oceanographers (Omstedt et al., 2014).

The Danish straits experience alternating inflow and outflow events. These events are irregular and predominantly driven by changes in atmospheric forcing (Lass & Matthäus, 2008). The high spatial and temporal variability makes quantification of the exchange from models and in situ observations rather difficult. The volumetric flow rate is usually estimated based on semi-empirical models and in situ observation of sea level with the

barotropic assumption (Jakobsen et al., 2010; Mattsson, 1996). This approach assumes a constant velocity across the strait and often neglects the baroclinic, the wind and the tidal contributions.

In situ observations of ocean currents are localized, sparse and costly. In addition, they usually do not cover the upper 10 m. Satellites are cost-effective tool to observe ocean surface currents. Spaceborne altimeters measure large-scale geostrophic currents, which are often not correlated with small-scale sea surface height anomalies. While the geostrophic assumption generally holds in the open ocean, it becomes less reliable in coastal areas and shelf seas. Additionally, conventional nadir altimeters are limited by their coarse spatial resolution, restricting them to detecting surface currents at scales of around 100 km. Wide-swath altimeters such as SWOT can resolve finer scales, down to 15–30 km (Morrow et al., 2019). However, during its nominal phase, with a 21-day repeat orbit and a 120-km swath width, SWOT will have an average revisit time of 11 days, which is comparable to that of a single-satellite SAR. Surface currents can also be derived from sequences of tracer fields, for example, SST, provided by satellite infrared images (Emery et al., 1986). This technique requires high-resolution cloud-free images with sufficiently short time difference (∼6 hr), which restricts its operational usability. Passive microwave based SST can also be used to infer sea surface currents (Isern-Fontanet et al., 2006). These data are weakly sensitive to clouds but the spatial resolution of the order 20–50 km limits their use in regional and local studies. Both techniques assume that the tracers are solely advected by the underlying current. A new promising technique based on optical sensors can provide currents with a spatial resolution of approximately 1 km but limited to favorable day-light and cloud-free conditions (Yurovskaya et al., 2019).

Synthetic aperture radar (SAR) offers the possibility to observe the sea surface circulation with very high spatial resolution. These high resolution observations are particularly relevant in coastal areas and shelf seas where the spatial scales are shorter than in the open ocean. SAR has been providing valuable information on sea surface winds and waves for many decades. During the last decade, a new application of SAR measurements based on the analysis of the Doppler shift has emerged (Chapron et al., 2005; Johannessen et al., 2008; Romeiser et al., 2005). The SAR Doppler shift is directly related to the sea surface motion, thus in principle direct measurements of surface currents is possible. It is however a challenging problem in practice. In addition to the instrument-related calibration inaccuracies (Hajduch et al., 2022; Moiseev et al., 2022), surface waves contribute to the observed Doppler shift, which must be accurately estimated and removed (Elyouncha et al., 2019; A. C. H. Martin et al., 2016; Moiseev et al., 2022).

The capability of SAR to resolve high-resolution ocean surface currents has been demonstrated in numerous works, for example, (Elyouncha et al., 2019; Wang et al., 2019). However, comparatively less attention has been devoted to examining the temporal evolution of these phenomena. Specifically, the capacity of SAR to resolve the temporal variations of sea surface current field remains largely unexplored and undocumented. This research endeavors to address this notable gap in knowledge. Despite SAR's high spatial resolution, spaceborne sensors, including SAR, typically exhibit poor temporal resolution. A primary constraint lies in the long revisit time (approximately 12 days) associated with spaceborne SAR missions. Overcoming this limitation requires the fusion of data acquired from multiple satellites, thereby introducing the challenge of integrating sensors operating at different frequencies and employing different imaging techniques. A recent study by (Elyouncha, Eriksson, & Johnsen, 2022) demonstrated that a good agreement between radial velocities derived from two independent spaceborne SAR systems, operating at distinct frequencies, can be achieved, provided that the data sets are well calibrated. This finding has inspired our approach, prompting us to synergistically utilize sea surface velocity estimates obtained from diverse C- and X-band spaceborne SAR systems.

The primary objective of this study is to assess the potential of multi-mission SAR in monitoring the inflow/outflow circulation dynamics between the Baltic Sea and the North Sea via the Danish straits. This assessment is conducted through the analysis of a time series of SAR-derived Doppler shift data. The study utilizes a 2-month data set (June and July 2020) comprising opportunistic SAR acquisitions covering the Danish straits, specifically the Fehmarn Belt. Furthermore, this study investigates the relationship between the surface currents along the Fehmarn Belt, the sea surface wind, and the sea level variations, with the aim of discerning the primary drivers of surface flow dynamics and their associated time scales. To address the temporal sampling constraints inherent in individual SAR missions, data from three satellite-borne SAR sensors, namely Sentinel-1A, Sentinel-1B, and TanDEM-X, are integrated. This integration aims to reduce the temporal sampling interval, thereby enhancing the temporal resolution of the observations.

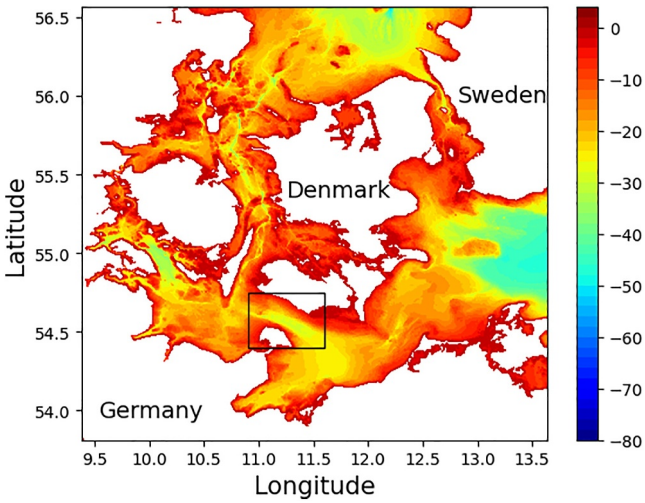

Figure 1. Study area is the transition area between the Baltic Sea (south east in the image) and the Kattegat Sea (north in the image). The black rectangle outlines the Fehmarn Belt, which is located between Denmark and Germany. Color is bathymetry (red shallow, blue deep).

2. Study Area and Data

2.1. Study Area

Figure 1 shows a map of the study area with the bathymetry color-coded from deep in blue and shallow in red. The channel outlined by the black rectangle, which is located in the south-west part of the Baltic Sea, is called the Fehmarn Belt. The channel is a relatively narrow (~20 km wide) and shallow (maximum depth of ~28 m). The Fehmarn Belt is an important channel for the exchange of water between the Baltic Sea and the North Sea (Gustafsson, 1997; Lass & Matthäus, 2008). The transport through the Fehmarn Belt is about 80% of the total transport, compared to the Öresund channel, with about 20% of the total transport (Mattsson, 1996). The salinity of the Baltic Sea is significantly affected by the water transported in the two routes (Feistel et al., 2008).

The flows through the Danish straits (Öresund and Fehmarn Belt) are mainly barotropic, driven by the prevailing meteorological conditions, which cause considerable water level variations in the North Sea and the Baltic (Fennel & Sturm, 1992; Jakobsen & Trébuchet, 2000). This results in flows into or out of the Baltic Sea of up to several days of duration, during which the water masses are advected through the straits. However, the horizontal density gradients caused by salinity differences between the different basins and the currents generated by the local wind may also contribute. Tidal waves are generally much smaller than the meteorologically induced water level variations.

The time period of our study is primarily constrained by the simultaneous availability of data from three different satellites, which is limited to two summer months. Circulation patterns during this period may differ from those in winter and may not fully represent the general circulation in the area. While the circulation in the study area varies over longer time scales, such as seasonal, annual, and decadal, our focus is on shorter time scales (a few days), which are more challenging to resolve from space. Longer time scales (>1 month) can be adequately captured by a single satellite.

2.2. Satellite Data

In this study, data from three satellite-borne SAR sensors are combined, namely Sentinel-1A (S1A), Sentinel-1B (S1B) and TanDEM-X (TDX). S1A and S1B are identical but the two systems (Sentinel-1 and TDX) differ in the imaging mode (TOPS and stripmap) and operating frequency (C-band, ~5 GHz and X-band, ~10 GHz).

S1A and S1B both carry conventional single-antenna SAR. The data used in this work are provided in the Sentinel-1 level 2 ocean (OCN) product in Interferometric Wide Swath (IW) mode (ESA, 2016). The OCN product contains three components: Ocean Wind field (OWI), Ocean Swell (OSW) and Radial Velocity (RVL). The RVL component, which is of interest here, contains mainly the Doppler centroid and the radial velocity (Engen & Johnsen, 2015). The spatial resolution of the OWI and RVL components is ~1 × 1 km.

TDX is an along-track interferometric SAR based on a formation of two satellites (TerraSAR-X and TDX), that is, a system of two satellites flying in tandem and carrying almost identical X-band SAR sensors (Krieger et al., 2007). The images used here are part of the Coregistered single look complex (CoSSC) data set (Duque, 2012). Note that TDX is not an ocean-dedicated mission. Only images acquired with short along-track baseline are suitable for ocean current retrieval. These acquisitions are rare and sporadic.

The study is based on the time period June and July 2020. This time period is constrained by the availability of coincident (Sentinel-1 and TDX) data covering the area of interest. During this period unique (with optimal along-track baseline) TDX images were acquired over the Fehmarn Belt. In this study, 30 S1A and S1B images in the format of OCN products freely provided by ESA and 8 SLC TDX images provided by DLR under a license agreement, were used. Note that we are focused here on the mesoscale and synoptic scales with time periods from 2 to 10 days. Thus the time span of the satellite data (2 months) should be sufficient to cover a few periods of interest. Finally, the processed Sentinel-1 and TDX data used in this work are archived and publicly available (Elyouncha & Johnsen, 2024).

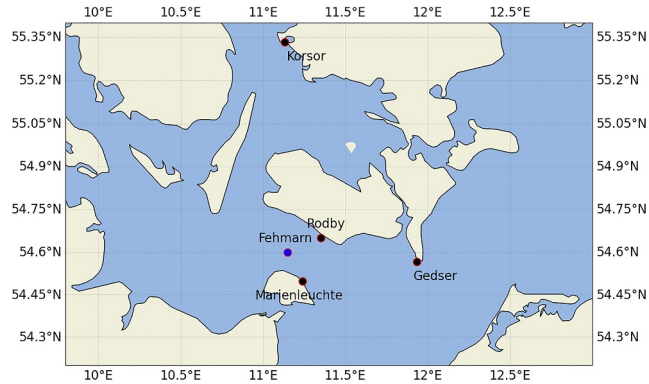

Figure 2. Locations of the in situ stations of current and sea level used in this study. The Fehmarn station measures sea current and wind. The stations Rodby, Marienleuchte, Gedser and Korsor measure sea level.

2.3. In Situ Data

A moored buoy located in the Fehmarn Belt (see Figure 2) operated by the Federal Maritime and Hydrographic Agency (BSH) measures wind speed and direction at 10 m height, and current speed and direction at 10, 15, 20 and 24 m depths. These in situ data, freely provided either by BSH and Copernicus, are used as a reference in this study. Since the in situ wind measurements cover only June 2020, it is complemented by the reanalysis wind data (ERA5) provided by the European Center for Medium-Range Weather Forecasts (ECMWF). A comparison (see Figure 3) of the ERA5 wind and the in situ wind measurements shows a very good agreement. This is not entirely surprising, considering that the ERA5 reanalysis product assimilates a vast amount of in situ marine wind data (Hersbach et al., 2020), though not necessarily from this specific station.

Four sea level (SL) gauges are used, namely Rodby, Marienleuchte, Gedser and Korsor. The locations of these tide gauges are shown in Figure 2. These provide measurements every 10 min, but they are down-sampled to hourly time series. These data is used to investigate the relationship between across-channel and along-channel sea level gradients and the along-channel current (see Section 4.2 for more details).

2.4. Model and Re-Analysis Data

For comparison, ocean model data produced by the Swedish Meteorological and hydrological institute (SMHI) using the NEMO−Nordic model, are used. The horizontal resolution of this model is 1 nautical mile. The vertical resolution at the surface layer is 1 m with up to 56 vertical depth levels. Satellite SST, ice concentrations and in situ temperature and salinity profiles are assimilated into this model. These data are provided by Copernicus under the product name BALTICSEA_ANALYSIS_FORECAST_PHY_003_006. A detailed description of the product can be found in Lindenthal et al. (2023). The current field and sea level derived from the NEMO-Nordic model are used for analysis and comparison with in situ and satellite data.

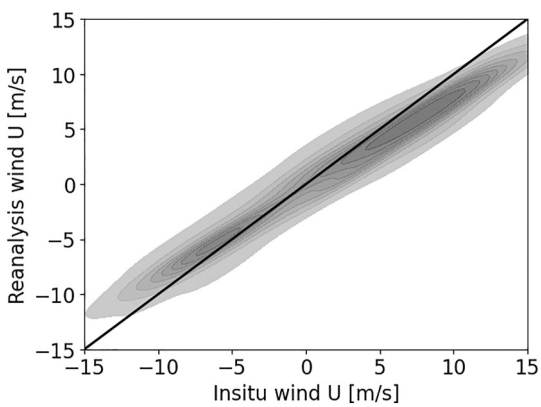

Figure 3. Comparison of the model wind (U component) and the in situ (Fehmarn station) wind (U component) during June–September 2020. Mean difference (Bias = 0.64 m/s); standard deviation of the difference (STD = 1.96 m/s); root mean squared error (RMSE = 2.06 m/s); mean absolute error (MAE = 1.68 m/s); median absolute deviation (MAD = 1.50 m/s); and Pearson correlation coefficient (R = 0.97).

Figure 4 shows the time series of the model and in situ current zonal component in the Fehmarn Belt. The positive values of the U component of the current correspond roughly to inflows (to the Baltic Sea) and negative values to outflows (from the Baltic Sea). It can be observed that the Fehmarn Belt experience irregular and alternating inflow and outflow events with episodes varying from 1 to 10 days. The current is very transient, that is, it can change speed and direction in time scales 1–3 days, which requires short time sampling and thus a priori challenging to monitor from space. It can be noticed that the model almost always overestimates the current speed with instantaneous relative errors that often exceed 100%. It can also be noticed that the model exhibits larger biases particularly during episodes where the vertical shear is strong, that is, difference between surface current and −10 m current is larger, which

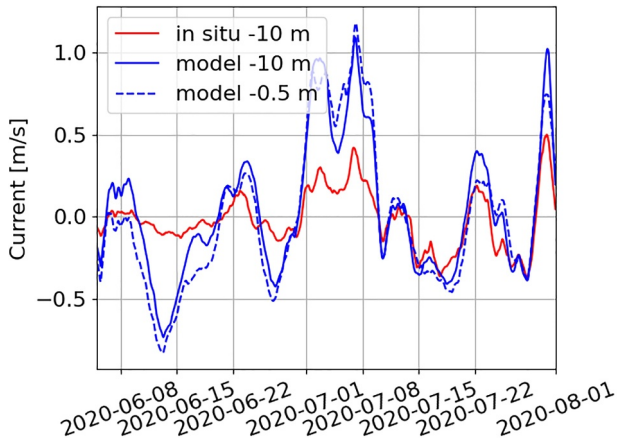

Figure 4. Time series of the ocean model current (U component) at 0.5 and 10 m depth and in situ current (U component) at 10 m depth at the Fehmarn Belt station.

may indicates dominantly local-wind-driven current episodes. In contrast, during episodes of dominantly sea-level-driven current and small vertical shear, which indicates a barotropic current, the model agrees quite well with the in situ measurements. Figure 5 depicts the comparison of the interpolated model current against in situ current. From the scatterplot, it can be seen the model is clearly skewed compared to the in situ measurements. Particularly the positive values (inflow) are significantly overestimated by the model.

Figure 6 depicts the sea level (color-coded) and the surface current vector (red arrow), at the Fehmarn Belt station, provided by the ocean model. An across-channel sea level gradient is clearly noticeable between the northern (Danish) coast and southern (German) coast of the Fehmarn Belt. It can also be noticed that the sea level gradient is consistent with the current direction (outflow), that is, geostrophic balance.

3. Methods

3.1. Radial Velocity Estimation From SAR Data

Basically, SAR measures the mean velocity of the surface scattering elements, averaged over the resolution cell and integration time, with each scattering element velocity weighted by its normalized radar cross section (NRCS) (Chapron et al., 2005; Johannessen et al., 2008). This mean velocity will induce a shift in the SAR image azimuth spectrum, also called Doppler spectrum, which would be centered around zero when a static surface is imaged (Thompson, 1989). The radial (velocity vector projected on the SAR line-of-sight) surface velocity is derived form the center of the azimuth spectrum, that is, Doppler centroid (DC). The dominant contribution to the DC is due to the wind wave orbital velocities.

The Doppler centroid can be estimated from SAR data using two major techniques, Along-track interferometry (ATI), which is only applicable to ATI systems such as TDX, and Doppler centroid anomaly (DCA), which is applicable to any conventional SAR, for example, Envisat, Sentinel-1. The DC is estimated from Sentinel-1 using the Doppler anomaly analysis method, for example, (Moiseev et al., 2020), while for TDX, it is estimated from the interferometric phase (Romeiser et al., 2005). The DC estimated by two methods are related by

$$f_{DC} = \frac{1}{2\pi}\frac{\phi_{ATI}}{\tau} = \frac{k_e}{\pi}V_r, \tag{1}$$

where V_r is the radial velocity (RVL) of the satellite relative to moving ocean surface. $V_r = V_h \sin\theta$, where V_h is the horizontal radial velocity and θ is the incidence angle of the electromagnetic wave. ϕ_{ATI} is the interferometric phase measured by an interferometric SAR such as TDX and τ is the along-track temporal baseline.

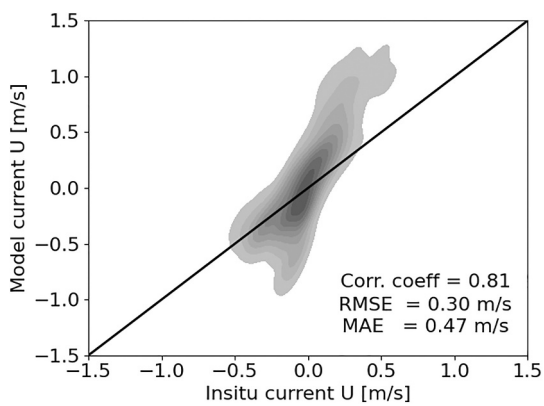

Figure 5. Comparison of the ocean model current against the in situ current (zonal component) at 10 m depth over June–July 2020.

The Doppler centroid can be virtually decomposed into different components attributed to different sources of motion

$$f_{DC} = f_{geom} + f_{phys} + f_{error} \tag{2}$$

where f_{geom} is due to satellite velocity relative to solid rotating Earth, which requires accurate orbital/attitude parameters (Moiseev et al., 2020). f_{phys} is due to ocean surface currents and waves. f_{error} groups all sources of errors. Usually Doppler calibration is needed to estimate f_{error}, which requires a reference (in height and velocity). In this work, the land is used as a reference (zero velocity) to calibrate the observed Doppler centroid. To get an idea how challenging it is to get accurate surface currents from SAR, if a precision of $\Delta V_h = 0.1$ m/s is required, it implies a Doppler precision of $\Delta f_{DC} = 3.7$ Hz, (X-band), $\Delta f_{DC} = 2.08$ Hz (C-band) at $\theta = 35°$.

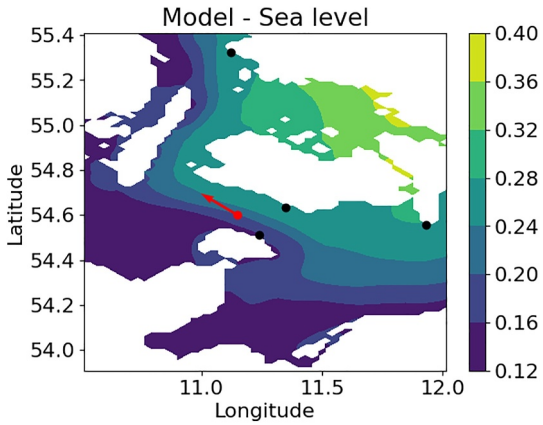

Figure 6. Model sea level and current (05-06-2020 00:29:00). The black dots represent the sea level gauges Gedser, Rodby and Korsor and the red dot represents the Fehmarn Belt buoy. The red arrow represents the model current interpolated to the location of the Fehmarn Belt buoy.

For Sentinel-1, the SLC-to-Doppler shift processing is performed by the S1-IPF Level 2 processor (Engen & Johnsen, 2015) and provided in the S1 OCN RVL product. In addition to the total observed Doppler shift, the OCN product contains the geometric and miss-pointing Dc. The geometric Dc is due to the satellite velocity relative to the solid rotating Earth. The miss-pointing DC is due to the antenna pattern skewness as a function of elevation angle.

For TDX, the SLC-to-Doppler shift processing is performed in house. An interferogram is formed using the two single-look complex (SLC) coregistered images. TDX is not a pure along-track interferometric system, but a hybrid (across- and along-track) interferometric SAR. Thus, the observed phase is sensitive to both topography and displacement. The topographic phase is removed using a geoid and a digital elevation model (DEM). To reduce the phase noise and increase the phase precision, the interferogram is multilooked, which downgrades the spatial resolution. The multilooked pixel size is about 100 m in ground range and azimuth. In order to be able to relate the interferometric phase to velocity, the phase must first be unwrapped. Once the interferogram is unwrapped, the DC and the radial velocity can readily be derived using Equation 1.

3.2. Wave-Induced Doppler Velocity Correction

The wave-induced DC is corrected using the empirical model CDOP and the semi-empirical model KaDOP proposed by Mouche et al. (2012) and Yurovsky et al. (2019), respectively. These models are often referred to as geophysical model functions (GMF). They take wind and wave parameters as input and return, ideally, the predicted DC that should be measured by SAR in absence of currents.

$$f_{DCwave} = GMF\left(U_{10}, \varphi_{10}, H_{ww}, T_{ww}, H_{sw}, T_{sw}\right) \tag{3}$$

where U_{10} and φ_{10} are wind speed and wind direction, respectively. H is the significant wave height, T the wave period, the subscripts *ww* and *sw* refer to wind waves and swell. Note that the CDOP GMF takes only wind speed and direction as inputs while KaDOP GMF takes into account all the parameters above. However, wave information was not available for this study. Thus both GMFs are fed with wind speed and direction obtained from ERA5 reanalysis data.

The removal of wave contribution consists of simply subtracting the predicted f_{DCwave} from the calibrated observed f_{DC}, assuming that the geometric f_{geom} and f_{error} are correctly removed through calibration. Note, that this approach assumes that the wave and current fields are independent and thus neglects the wave-current interaction.

3.3. Spectral Analysis

Spectral analysis is used here to determine how the energy in the oceanic processes governing the circulation in the study area is distributed in frequency domain and to identify the dominant frequencies and time scales. The Welch's method is used to calculate the current, wind and sea-level spectra. The linear trend was removed from the hourly time series. Values of sea level larger than 1 m were removed (replaced by interpolated values). Also missing values in all fields were replaced by linearly interpolated values for short gaps (a few hours). For wind and current vectors, the rotary spectrum (Li, 2022; Thomson & Emery, 2014) is calculated as the Fourier transform of the complex velocity $(u + iv)$.

The variance of the resolved (by satellites) and unresolved variability was estimated as the integral of the spectral density within the corresponding frequency band

$$\sigma^2 = \int_{f_1}^{f_2} S(f)df \tag{4}$$

where $f_1 = 0$ and $f_2 = f_{sat}/2$ for the variance resolved by the satellite, and $f_1 = f_{sat}/2$ and $f_2 = f_{\max}$ for the unresolved part of the spectrum. f_{sat} is the average revisit rate of the satellite combining S1A, S1B and TDX. df is the frequency bin and $f_{\max} = 12$ cpd (cycle per day) is the maximum frequency. The former frequency range corresponds roughly to the synoptic scale from 2 to 30 days and the latter to the mesoscale from 2 hr to 2 days.

3.4. Correlation Analysis

The correlation analysis is carried out through the auto-correlation of current and sea level and the cross-correlation between the current and sea level and wind. The standard definitions of the auto- and cross-correlation functions (Thomson & Emery, 2014) are used here. Both the decorrelation time and the integral time scale are calculated for each autocorrelation function. The integral timescale, T^*, is defined as the integral of the autocorrelation function (Thomson & Emery, 2014)

$$T^* = \int_0^{\tau_0} R(\tau) d\tau \tag{5}$$

Here, the autocorrelation function $R(\tau)$ is integrated only to the first zero crossing τ_0.

3.5. Vector Projection

3.5.1. Projection Along- and Across-Strait

For analysis of the driving forces (Section 4.2), the current and wind vectors are projected along and across the strait, that is, the vector fields are rotated, such that the along-channel current is parallel to the shoreline and perpendicular to the across-channel sea level difference between Rodby and Marienleuchte stations (see Figures 2 and 6). The along-channel U_{al} and across-channel U_{ac} are calculated as

$$U_{al} = -U \sin(\alpha) + V \cos(\alpha), \tag{6}$$

$$U_{ac} = U \cos(\alpha) + V \sin(\alpha), \tag{7}$$

where $\alpha = \pi - \beta$ and β is the bearing angle from north to the along strait direction clockwise. U and V are the zonal and meridional components of the current or wind vectors.

3.5.2. Projection on the SAR LOS

As is known SAR measures only the radial component of the surface velocity. Thus for comparison, the wind, model current and in situ current vectors are projected on the SAR line-of-sight (LOS) as

$$U_r = -\left(\vec{U} \cdot \vec{L}\right) \tag{8}$$

where U_r is the radial component, U is wind or current vector in the geographical coordinates and L is the SAR unit look vector pointing from the nadir to the imaged point on the sea surface, that is, along the ground range. $\vec{L} = [\cos(\alpha), \sin(\alpha)]$ in ascending pass and $\vec{L} = [-\cos(\alpha), \sin(\alpha)]$ in descending pass, $\alpha = (360 - h)$ and h is the heading angle of the satellite relative to north. The minus sign keeps the traditional convention, that is, positive velocity when wind or current is moving toward the radar antenna and negative sign for the opposite direction.

3.5.3. The Geostrophic Current

The theoretical geostrophic current is used here only for comparison with model and in situ data in Section 4.2. It is calculated as

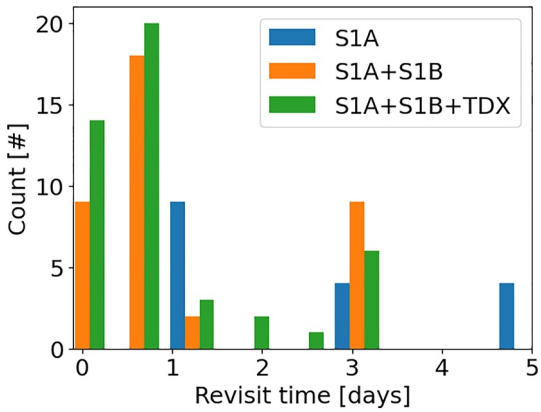

Figure 7. Distribution of the satellite revisit time (time difference between consecutive acquisitions) for different combinations of platforms, at the Fehmarn Belt during June–July 2020.

$$V_G = \frac{g}{f}\frac{\partial \eta}{\partial x} \tag{9}$$

where f is the Coriolis parameter, g is the acceleration due to gravity, η is the sea level and x is the across-strait distance.

4. Results

4.1. Satellite Revisit Time

The repeat cycle (the time between two successive identical orbits) of a satellite is determined solely by the orbit altitude with higher altitudes leading to longer repeat cycles. The revisit time (the interval between subsequent images of the same area) is influenced by orbit altitude, swath width, and the spacing between consecutive ground tracks, which decreases with latitude as the tracks converge. As a result, revisit time increases with satellite altitude but decreases with latitude, meaning high-latitude areas are imaged more frequently than low-latitude areas due to the overlap between adjacent swaths. Additionally, spaceborne SAR missions are not continuously acquiring images and are often not dedicated solely to ocean observation, which further increases the revisit time, as not every pass results in an image.

Sentinel-1 is in a near-polar, sun-synchronous orbit with a 12 days repeat cycle for a single satellite. Both S1A and S1B share the same orbit plane with a 180° orbital phasing difference. With both satellites combined, the repeat cycle is 6 days. TDX is also near-polar, sun-synchronous orbit. Its repeat cycle is 11 days due to slightly lower altitude (514 km) than Sentinel-1 (693 km). The total number of Sentinel-1 acquired SLC images in June and July covering the Fehmarn Belt is 39, but they are not all processed to OCN products and even those processed are not all of good quality, that is, some images are very noisy. The final useful number of Sentinel-1 images is 30.

Figure 7 shows the distribution of the revisit time, calculated as the difference between consecutive satellite acquisitions, during June and July 2020. This presents the real actual time difference between images. It is clear that with one satellite for example, S1A, all images are acquired with more than a day difference, while by combining more satellites the revisit time decreases to subdaily intervals. The mean revisit time is 3.14 days, for S1A alone, 1.48 days for S1A & S1B and 1.22 days for S1A, S1B & TDX. The achieved median revisit time is 1 day. Note that TDX is not meant to operate in a constellation with Sentinel-1 orbit so the phasing is not optimal nor regular. Thus adding the TDX to the constellation only slightly reduces the mean revisit time.

4.2. Dominant Processes and Time Scales of Variability

The objective of this section is to identify the time scales of the oceanic and meteorological processes driving the flow along the Fehmarn Belt. Note that the purpose here is not to carry out a thorough investigation of the driving forces of the oceanic processes in the study area. The main purpose is to investigate if the time scales of the dominant processes can be resolved by satellite SAR. The reader interested in the driving forces can refer to (Jakobsen & Trébuchet, 2000; Jakobsen et al., 2010).

4.2.1. Spectral Analysis

Figure 8 shows the spectra of the current (panel a), the sea level difference (panel b) and the wind (panel c). The vertical dashed lines depict the average satellite revisit time, the M2 tidal component and the inertial frequency (see legend). The inertial period at the Fehmarn station is 14.7 hr and the M2 period is 12.4 hr. The three spectra exhibit strong and broad peaks at the synoptic scale between 2 and 20 days. In addition, the SL spectrum shows a noticeable M2 tidal peak. This tidal peak is very small but can be also seen in the current spectrum, which indicates that the tide penetrates down to 10 m depth, indicating barotropic flow. The main purpose of the spectral analysis done here is to notice that the average satellite revisit time is able to resolve most of the spectral content. Quantitatively, by applying Equation 4, it can be found that 89% of the spectral power is resolved by the three satellites combined and only 11% of the spectrum remains unresolved.

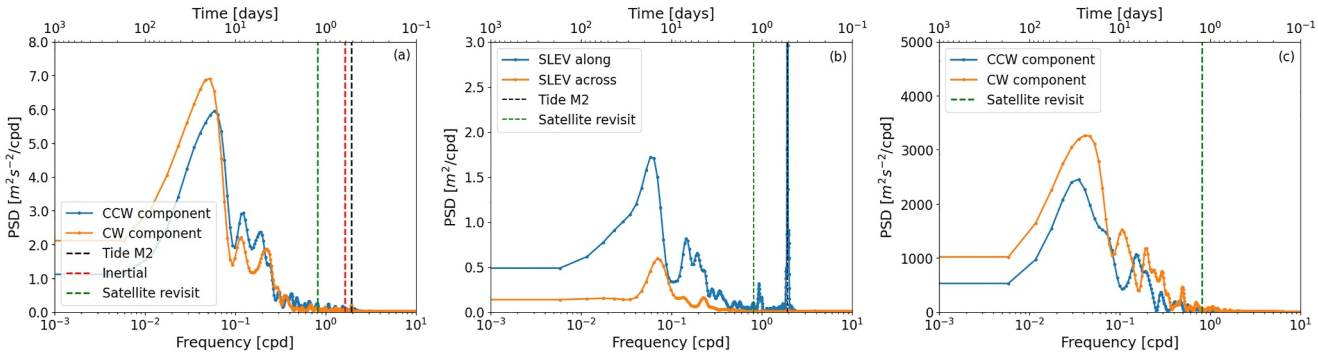

Figure 8. (a) Rotary spectra of the in situ current (U and V components) at −10 m in the Fehmarn Belt, (b) Spectra of the in situ sea level difference across- (Marienleuchte—Rodby) and along (Gedser—Korsor) the channel. (c) Rotary spectra of the wind vector ECMWF/ERA5 re-analysis (u_{10}, v_{10}).

4.2.2. Temporal Correlation

Figure 9 (panel a) depicts the autocorrelation function as a function of days for the across- and along-channel SL difference and the along-channel current. The decorrelation time (the e-folding), that is, the time at which the autocorrelation function is equal to 1/e, is calculated from the autocorrelation function. It is found that the decorrelation time is 2.79, 2.04 and 2.25, 1.83 days for across-channel SL, along-channel SL; and the along-channel current and wind, respectively. The integral timescale, $T*$, calculated with Equation 5 yields 2.6, 2.1, 2.2 and 2.9 days for the Across-, along-channel SL; and the along-channel current and wind, respectively.

Figure 9 (panel b) depicts the cross-correlation of the along-channel current with the three potential driving forces, that is, across- and along-channel SL difference and the along-channel wind. It can be noticed that there is a small lag between the across-channel SL difference and current (3 hr) due to geostrophic balance, while there is a lag of 54 hr between the along-channel SL difference and the current. This corresponds approximately to the time it takes the barotropic wave to propagate through the strait from Korsor to Gedser. The lag between the current and the wind is 42 hr, which his probably a combination of the wind-induced sea level gradient and the Ekman transport.

4.2.3. Multiple Regression

Figure 10 shows scatterplots of the along-channel current against across-channel SL difference obtained from the ocean model (panel a) and from in situ measurements (panel b). The across-channel sea level gradient is calculated as (η_{Rodby}—$\eta_{Marienleuchte}$). The theoretical geostrophic current (Equation 9) is also plotted on the scatter plots for comparison. High correlation is observed between the along-channel current and the across-channel SL difference. The geostrophic balance line fits well the data for both the model and the in situ measurements. This suggests that the geostrophic balance is an important process in the Fehmarn Belt upper layer circulation. This

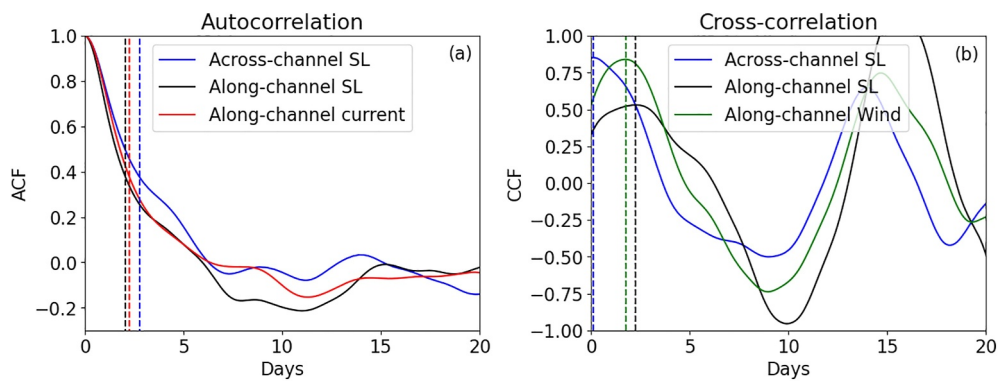

Figure 9. Autocorrelation function (a) of along- and across-channel SL difference and the along-channel current, cross-correlation (b) of the along-channel current with SL difference and wind.

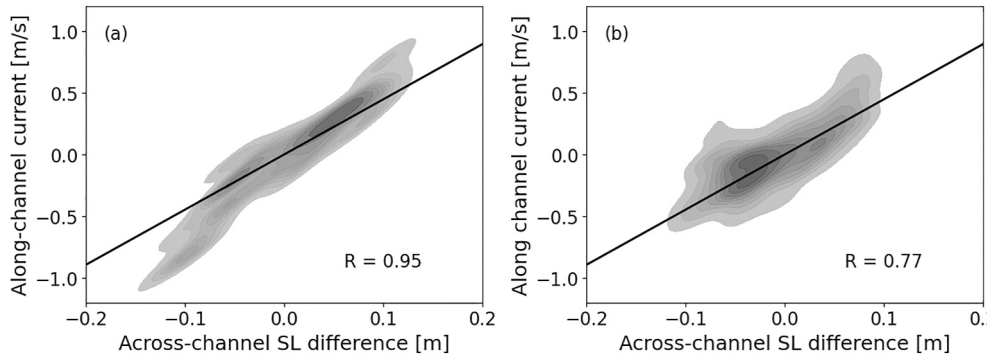

Figure 10. Scatterplots of the ocean model along-channel surface current against across-channel SL difference (Rodby—Marienleuchte), ocean model (a), in situ (b). Positive current is outflow and negative is inflow. The black line is the geostrophic current (V_G) calculated from the SL difference using Equation 9.

process has time scales (excluding the semidiurnal tidal component) larger than 2 days (see Figure 8), hence resolvable by the three satellite constellation. The deviation of the model current from the geostrophic current at negative values might suggest other contributions to the current such as wind- and density-driven circulation.

Multiple regression analysis has been carried out to quantitatively determine the partial contribution of each potential driving force, that is, along-channel SL difference, across-channel SL difference, wind and tide, to the along-channel current. The results are summarized in Table 1. It is found that the across-channel sea level gradient accounts for 53% of the variance, along-channel sea level gradient 27% and the local wind 20%, while the tide contribution is negligible. Note that individual forcing contributions may covary (colinearity), for example, wind an SL. Such covariation makes it difficult to separate the forcing contributions using traditional multiple regression analyses. Thus, the explained variances should be taken as rough indication of relative contribution. Nevertheless, it is clear that along-channel flow is dominantly geostrophic and the tidal contribution can be neglected.

4.3. Satellite Derived Radial Velocity

In this section, the satellite SAR-derived radial velocity (RVL) is averaged over a small area around the in situ current station (Fehmarn Belt). The ERA5 wind components (U,V) are interpolated in time and space at the satellite acquisition time and the in situ station location, respectively. For current comparison, the in situ current measurements are interpolated at the satellite acquisition time. Thus, each point in the time series and scatter plots presented below is an average of a portion of the SAR image around the in situ current station (Fehmarn Belt).

First, the satellite SAR-derived RVL is compared against the radial wind speed (projection of the wind vector on the SAR line-of-sight). Second, the wave-corrected SAR RVL, which represents the SAR-derived radial current, is compared against in situ and model current. The radial velocity derived from both Sentinel-1 and TDX require absolute calibration. The results presented here are produced after calibration, using land as a reference. This calibration ideally removes all orbit- and instrument-related biases.

4.3.1. Before Wave Contribution Removal

Figure 11 shows the time series of the calibrated total (before wave correction) SAR-derived RVL and the simulated wave-induced Doppler velocity using the CDOP and KaDOP GMFs (called U_{cdop} and U_{kadop} in the plot) with the wind vectors provided by ECMWF/ERA5 used as input to the GMFs. The left panel shows the RVL derived from S1A and S1B. The right panel depicts the RVL derived from TDX. It can be noticed, from both panels, that the total SAR-observed RVL is highly correlated with the radial wind speed, which indicates that the wind (actually wind-waves but the wind is used as a proxy) is the dominant contribution to the total RVL. In contrast, the current is often a minor contribution except in cases with strong currents and low wind. This wind dominance makes the separation of the two contributions (waves and

Table 1
Multiple Regression Results

	Across SL diff	Along SL diff	Wind	Tide
R^2	0.57	0.29	0.21	0.0015
% of explained variance	53	27	20	0.15

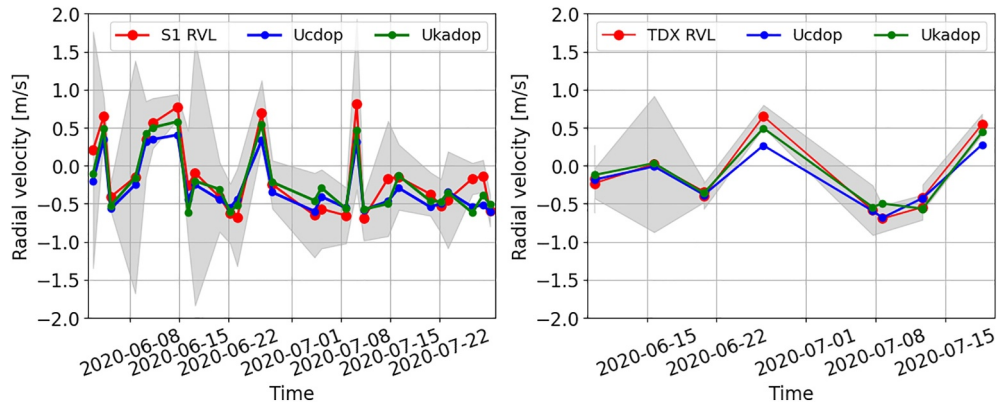

Figure 11. Time series of the SAR-derived total radial velocity (before wave correction). S1A and S1B (left panel), TDX (right panel). U_{cdop} and U_{kadop} are the wave-induced RVL simulated using the CDOP and KaDOP GMF, respectively. The shaded areas depicts the ± standard deviation.

currents) and hence the retrieval of surface currents from SAR challenging. The shaded area depicts the ± standard deviation. Since the radar signal-to-noise ratio (SNR) depends on the amount of the backscattered power from the ocean surface, higher wind speed increases the radar SNR and decreases the DC random error. Hence the higher uncertainty at low wind speed.

Figure 12 depicts the RVL obtained by combining the three satellites S1A, S1B and TDX. The time series resolves abrupt variations in wind-wave direction. It can be noticed how some gaps are filled by combining the three satellites. For instance, the positive peak around 17-07-2020, indicating a rapid wind inversion, would not have been resolved without the addition of TDX.

Figure 13 shows the scatterplots of the RVL derived from S1A and S1B (a), TDX (b) and the three satellites combined (c), against the radial wind speed. The high correlation coefficients (R> 0.9), suggests again the dominant contribution of wind-waves to the SAR-derived RVL. It also indicates that the current contribution is small, which consists of the small positive and negative deviations from the quasi-linear relation between the relative wind and the RVL. This relation is what the Doppler GMFs (CDOP and KaDOP) predict. In addition to the radial wind, it depends also on the incidence angle. Thus, part of the scatter is due to the fact that the SAR images have different incidence angles and probably also due to the difference in frequency bands (C- vs. X-band).

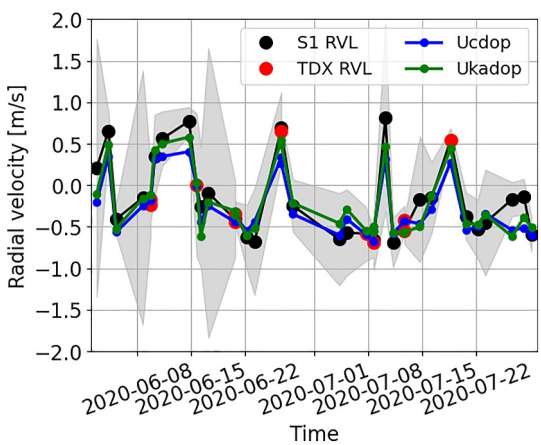

Figure 12. Time series of the SAR-derived radial velocity (before wave correction). S1A, S1B (blue circles) and TDX (red circles) combined. U_{cdop} and U_{kadop} are the wave-induced RVL simulated using the CDOP and KaDOP GMF, respectively. The shaded areas depicts the ± standard deviation.

4.3.2. After Wave Contribution Removal

In this section, the wave-induced Doppler velocity, calculated using the Doppler GMFs CDOP and KaDOP, is subtracted from the total RVL. Figure 14 shows the derived radial current, that is, after removing the wave bias from the total radial velocity, together with the in situ and the ocean model current, both projected on the SAR line-of-sight. First, it can be observed that the SAR-derived current follows well the temporal variation of the in situ measured current. Second, the SAR-derived current is almost always closer to the reference (in situ) than the model current. It can also be observed that when the model current exhibits large deviations from the in situ current, which is for instance noticeable between the 01-07-2020 and 08-07-2020, where the model exceeds the reference by more than 50%, the SAR-derived current has smaller deviations. This is an encouraging result, suggesting that ocean models could benefit from assimilating SAR-derived currents to mitigate their biases. Alternatively, current estimates could be improved by optimally blending model outputs with SAR retrievals, as demonstrated in studies such as (Elyouncha et al., 2021).

Figure 15 shows scatterplots of the model radial current versus the in situ current (panel a), and the SAR-derived current against the in situ current using

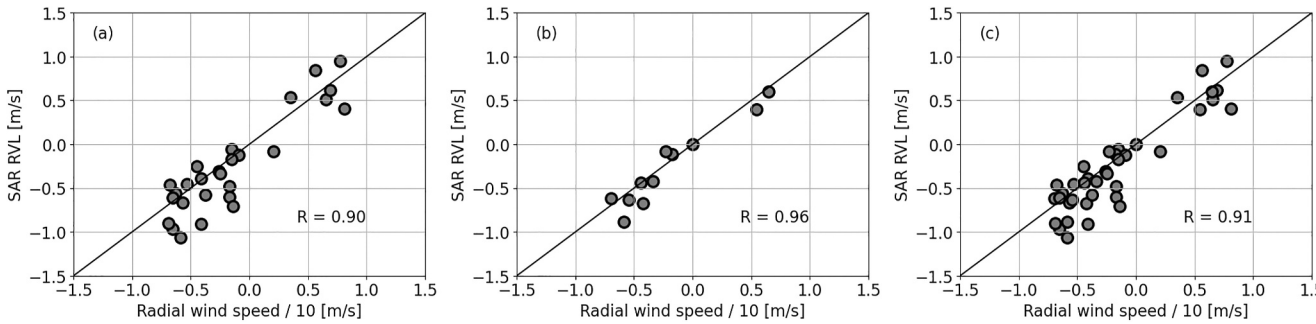

Figure 13. SAR-derived RVL (before wave correction) against radial wind speed. (a) S1A and S1B, (b) TDX, (c) S1A, S1B & TDX combined. *R* is the correlation coefficient.

two different GMFs to correct for the wind waves contribution, namely CDOP (panel b) and KaDOP (panel c). As observed earlier in the time series, the ocean model significantly overestimates the current in the inflow direction (positive velocity), where the current is not in geostrophic balance (see Figure 10). The model also overestimates slightly the current in the outflow direction (negative velocity). The SAR-derived current is slightly sensitive to the Doppler GMF used to correct for wave contribution, that is, CDOP (panel b) and KaDOP (panel c) give slightly different results. Note the difference between Figures 5 and 15a. Figure 5 is for the whole hourly data set June–July, while Figure 15a is only at the satellite acquisition times.

The statistics of the comparison are summarized in Table 2. Interestingly, the two corrections yield a correlation coefficient comparable to the ocean model. KaDOP yields the lowest bias followed by the model and CDOP. However, both GMFs yield systematically lower std, rmse, mae and mad than the ocean model, with KaDOP having a slight advantage over CDOP notably by the lower bias. The bias given by the CDOP correction might indicate a bias in the GMF since same wind was used as input to both GMFs. Additional residual differences (between SAR and in situ) might be due to other sources of error such as inaccuracies in the wind input used for wave bias correction and the natural difference between ocean current at the surface (observed by SAR) and −10 m (observed in situ).

5. Discussion

This study aims at investigating the capability of spaceborne SAR in discerning the temporal dynamics of ocean surface circulation within the Fehmarn Belt area. This includes determining dominant time scales of the ocean surface dynamics in the area, the optimal number of satellites required to adequately resolve these dominant time scales, and to quantify the achieved accuracy of the SAR-derived radial current.

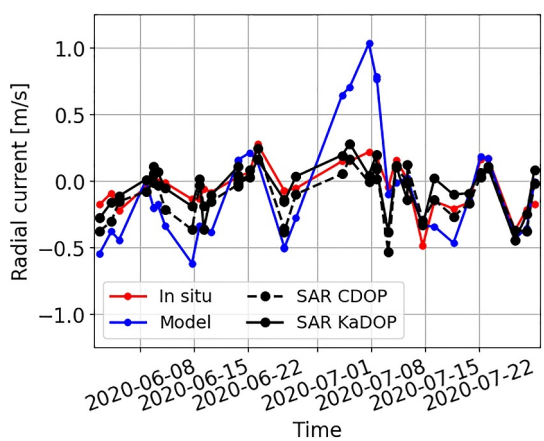

Figure 14. Time series of the SAR-derived radial current (after wave contribution removal) combining Sentinel-1 and TDX. Using KaDOP (black solid curve) and CDOP (black dashed curve) for wave correction. Red curve: in situ radial current; blue curve: model radial current. The dots correspond to the satellite acquisition times.

The study investigates the relationship between the surface current along the Fehmarn Belt, the sea level (along- and across-channel) and the surface wind, to determine the main driving forces of the surface flow and their dominant time scales. First, a high variability in the duration of inflow/outflow is observed, ranging from 1 day to 10 days. Second, it is found that the correlation between across-channel SL gradient and the flow is the strongest, followed by the along-channel SL gradient and the wind. The tide contribution is negligible. Though these observations agree with previous studies (Fennel & Sturm, 1992; Gustafsson, 1997; Jakobsen & Trébuchet, 2000; Mattsson, 1996), caution should be taken when it comes to drawing firm conclusions concerning the driving forces. Nevertheless, it is clear from this investigation that the time scales of the dominant processes in the area of interest are larger than 2 days.

It is shown that the dominant time scales can be resolved by combining at least three satellites. It has been demonstrated that satellite SAR is capable of monitoring the synoptic scale variation of the surface flow of the Baltic Sea

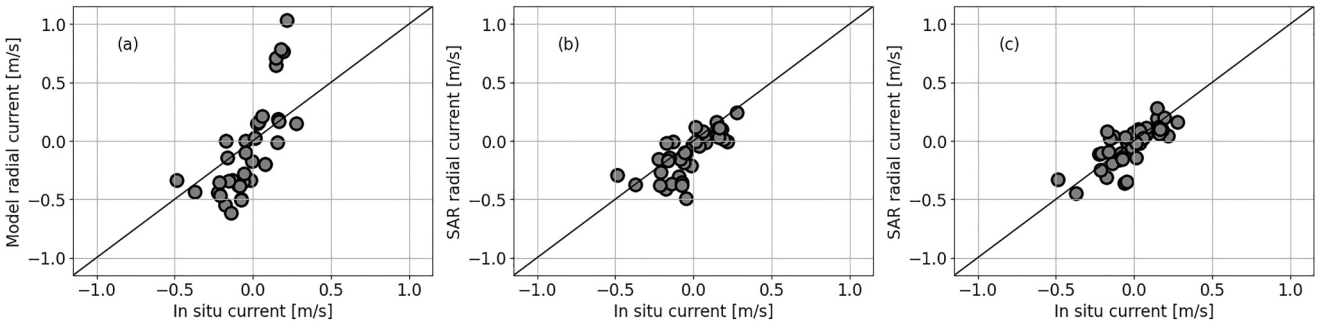

Figure 15. SAR-derived radial current versus in situ measured radial current. (a): Model current. (b): SAR using CDOP for wave correction. (c): SAR using KaDOP for wave correction.

through the Fehmarn Belt. Using the synergy between three satellites enhances the temporal sampling and consequently reduces the revisit time from 3.1 days using S1A alone, 2.8 days using S1B alone, 1.5 days using S1A & S1B to 1.2 days using S1A, S1B & TDX. The combined satellite data is able to resolve processes that have time scales larger than twice the average revisit time, that is, 2.4 days.

It is also shown that the SAR-derived total calibrated RVL, before wave correction, is highly correlated ($R \geq 0.9$) with radial wind speed and weakly correlated with the sea surface current ($R \approx 0.49$, not shown). This agrees with previous studies, for example, (Elyouncha, Eriksson, Romeiser, & Ulander, 2022; Moiseev et al., 2022). After wave bias correction, the correlation coefficient with in situ radial current is improved to achieve $R \approx 0.74$ and the rmse is reduced to 0.15 and 0.12 m/s using CDOP and KaDOP GMFs, respectively. These values of correlation are comparable to those found in a comparison of S1A data against high frequency coastal radar currents (A. C. Martin et al., 2022; Moiseev et al., 2020). The values of rmse found here (~0.15 m/s) are however lower than in Moiseev et al. (2020) and A. C. Martin et al. (2022) (~0.25 m/s), which is probably due to a lower accuracy of HF radar compared to in situ measurements used here. Note that empirical Doppler models such as CDOP and KaDOP primarily rely on the relationship between wind and Doppler radar measurements, under the assumption that these Doppler measurements are solely due to the orbital velocities of wind-waves. However, since the observed Doppler shift might also include contributions from wind-driven currents, using these models to correct for wave effects likely results in the removal of a portion of the wind-driven (Ekman) current.

It is found that the wave bias correction is sensitive to the Doppler GMF used, for example, CDOP and KaDOP GMFs give slightly different results, and to the input (wind and/or waves) to the Doppler GMF. Note that these GMFs have been derived for different radar systems operating at different frequencies C-band (CDOP) (Mouche et al., 2012) and Ka-band (KaDOP) (Yurovsky et al., 2019). Moreover, KaDOP was trained in the semi-enclosed Black Sea, where sea state conditions are more similar to those of the Baltic Sea. In contrast, CDOP was trained using data from the global ocean. Similar conclusions have been reported in Elyouncha et al. (2019) and A. C. Martin et al. (2022) regarding the sensitivity of current retrieval to the Doppler GMF by applying different GMFs to TDX and Sentinel-1 data, respectively. The sensitivity to wave bias correction through errors in the wind input and to inaccurate Doppler GMF CDOP and KaDOP GMFs need to be assessed further. The validity of the Doppler models at low (<25°) and high (>45°) incidence angles needs to be investigated.

Table 2
Statistics of Radial Current Retrieval Versus In Situ Measurements for Different Doppler Models

	Bias	Median	STD	RMSE	MAE	MAD	R
Model	0.03	0.10	0.31	0.31	0.24	0.20	0.73
CDOP	0.08	0.06	0.13	0.15	0.11	0.08	0.73
KaDOP	0.01	0.03	0.12	0.12	0.10	0.07	0.75

Note. Rows show: values for the ocean model, CDOP and KaDOP. Columns show: mean difference (Bias); standard deviation of the difference (STD); root mean squared difference (RMSE); mean absolute error (MAE); median absolute deviation (MAD); and Pearson correlation coefficient (R).

Evaluating the accuracy of current retrieval from SAR is challenging due to multiple sources of uncertainty. These include: (a) the estimated DC from SAR complex data, which is influenced by satellite orbital parameters such as attitude; (b) the Doppler GMF used to correct for the wave contribution; and (c) the wind vectors input into the GMF. Furthermore, uncertainties in satellite acquisition parameters, such as incidence and azimuth angles, can also impact the accuracy of current retrieval.

The accuracy of current retrievals can be assessed through direct comparison with reference data. This accuracy is typically quantified by calculating the bias and root mean square error, which correspond to the mean and the square

root of the average squared difference between the retrievals and the reference data, respectively. Additional metrics may also be used to evaluate accuracy. In this study, in situ current measurements from a moored buoy were used as the reference data. Other studies, for example, (A. C. Martin et al., 2022; Moiseev et al., 2020), have used HF coastal radars as a reference. It is assumed that the reference data is bias free and there is no significant difference between the surface current and the depth at which the in situ current is measured. Thus, the standard deviation and rmse reported in Table 2 (0.12–0.15 m/s) would correspond to the retrieval accuracy if these assumptions are valid, otherwise they should be considered as an approximation of the accuracy.

The SAR-current accuracy can also be estimated via simulation, by perturbation of the wind vectors and evaluation of the induced errors in the retrieved current. This method requires an assumed DC uncertainty, which can be for instance estimated from data acquired over land. Values of standard deviation estimated from C-band Envisat/ASAR data of ∼5–7 Hz have been reported (Hansen et al., 2011; Mouche et al., 2012). Similarly, values ranging from 6.45 to 9.67 Hz were estimated from X-band TDX data (Elyouncha et al., 2019) (see their Table 3). Following this method, the accuracy of the current speed retrieval at X-band was estimated to be lower than 12.5 cm/s for all wind speeds (Elyouncha et al., 2021) (see their Figure 22). Similar simulation (A. C. Martin et al., 2018) yielded an accuracy of ∼0.1 m/s at Ku-band. These values are close to the values found in this work.

6. Conclusion

This paper demonstrates that the combination of data obtained from three spaceborne SARs results in an average multi-satellite revisit time of 1.2 days, which proves sufficient for resolving surface circulation patterns within the Fehmarn Belt region. Furthermore, it is illustrated that the radial currents derived from SAR data exhibit a strong correlation (with a coefficient exceeding 0.7) when compared to in situ current measurements used as a reference. The achieved rmse, calculated based on the difference between the retrieved currents and the reference data, exhibits a slight dependency on the GMF used for wave correction but remains below 0.15 m/s. This represents a significant enhancement in accuracy compared to the ocean circulation model data, which yields an rmse of 0.31 m/s. Consequently, there appears to be considerable potential in assimilating SAR-derived radial currents into ocean circulation models. The promising outcome of this study not only highlights the feasibility but implies that numerous geographical regions exhibiting similar dynamics can be effectively monitored through the utilization of multi-mission SAR.

Despite the relatively limited temporal coverage of the data set employed in this study (spanning 2 months), our investigation clearly demonstrates the considerable potential of SAR for monitoring sea surface flows. However, to ensure a robust verification of these findings, a comprehensive analysis should be supported by an extended data set covering a longer temporal period, for instance, spanning 1 year. The optimal integration of model outputs with SAR-derived velocity fields holds promise for enhancing the accuracy of current flow estimations. The growing number of satellite SAR missions is expected to markedly reduce revisit intervals, thereby facilitating the resolution of previously unexplored time scales and rendering temporal analysis of SAR data not only feasible but also invaluable for comprehensive oceanic monitoring across both high temporal and spatial scales.

Finally, we believe these findings are relevant for spaceborne radar missions, including SAR and scatterometer, dedicated to measuring ocean surface winds and currents. Missions such as ODYSEA (Rodríguez et al., 2019; Torres et al., 2023) and Harmony (ESA, 2022) could benefit from our insights, potentially leading to advancements in oceanographic observation and analysis.

Data Availability Statement

This study has been conducted using the European Centre for Medium-Range Weather Forecasts (ECMWF) Reanalysis v5 (ERA5) data (Hersbach et al., 2018) and the E.U. Copernicus Marine Service Information (CMEMS) data (Lindenthal et al., 2023; TAC, 2023). Sentinel-1 and TanDEM-X data sets, processed by the authors, are available in Elyouncha and Johnsen (2024). Data analysis was performed in Python. For reading the netcdf files and interpolation we used the Xarray package, available at https://docs.xarray.dev. The spectra were calculated using the scientific computing package for Python (SciPy), available at https://docs.scipy.org. The correlation analysis performed using the statsmodels package, available at https://www.statsmodels.org. Figures were made with Matplotlib available under the Matplotlib license at https://matplotlib.org/. The Python code used to produce the results and the plots in this manuscript is published in Elyouncha (2024).

Acknowledgments
This work was funded by the Swedish National Space Agency (SNSA) contracts dnr 214/19 and dnr 2023-00178. Data for TanDEM-X and Sentinel-1 were provided by the German Aerospace Center (DLR) and the European Space Agency (ESA), respectively. Wind and ocean model data were provided by ECMWF and CMEMS, respectively. We would like to thank, SNSA, DLR, ESA, CMEMS and ECMWF. We would like also to thank Johnny A. Johannessen and Artem Moiseev at Nansen Environmental and Remote Sensing Center (NERSC, Bergen, Norway) for useful and interesting discussions.

References

Chapron, B., Collard, F., & Ardhuin, F. (2005). Direct measurements of ocean surface velocity from space: Interpretation and validation. *Journal of Geophysical Research*, *110*(C7), C07008. https://doi.org/10.1029/2004JC002809

Duque, S. (2012). *TanDEM-X payload ground segment—CoSSC generation and interferometric considerations (Tech. Rep.)*. DLR.

Elyouncha, A. (2024). Python script used to produce the results and plots in manuscript AGU 2024 [Software]. *Zenodo*. https://doi.org/10.5281/zenodo.10992561

Elyouncha, A., Eriksson, L. E., Broström, G., Axell, L., & Ulander, L. H. (2021). Joint retrieval of ocean surface wind and current vectors from satellite SAR data using a Bayesian inversion method. *Remote Sensing of Environment*, *260*, 112455. https://doi.org/10.1016/j.rse.2021.112455

Elyouncha, A., Eriksson, L. E. B., & Johnsen, H. (2022a). Direct comparison of sea surface velocity estimated from sentinel-1 and TanDEM-X SAR data. *Ieee Journal of Selected Topics in Applied Earth Observations and Remote Sensing*, *15*, 2425–2436. https://doi.org/10.1109/JSTARS.2022.3158190

Elyouncha, A., Eriksson, L. E. B., Romeiser, R., & Ulander, L. M. H. (2019). Measurements of sea surface currents in the Baltic Sea region using spaceborne along-track InSAR. *IEEE Transactions on Geoscience and Remote Sensing*, *57*(11), 8584–8599. https://doi.org/10.1109/TGRS.2019.2921705

Elyouncha, A., Eriksson, L. E. B., Romeiser, R., & Ulander, L. M. H. (2022b). Empirical relationship between the Doppler centroid derived from X-band spaceborne InSAR data and wind vectors. *IEEE Transactions on Geoscience and Remote Sensing*, *60*, 1–20. https://doi.org/10.1109/TGRS.2021.3066106

Elyouncha, A., & Johnsen, H. (2024). Sentinel-1 and TanDEM-X SAR data—Fehmarn belt [Dataset]. *Zenodo*. https://doi.org/10.5281/zenodo.10974142

Emery, W. J., Thomas, A. C., Collins, M. J., Crawford, W. R., & Mackas, D. L. (1986). An objective method for computing advective surface velocities from sequential infrared satellite images. *Journal of Geophysical Research*, *91*(C11), 12865–12878. https://doi.org/10.1029/JC091iC11p12865

Engen, G., & Johnsen, H. (2015). *Sentinel-1 Doppler and ocean Radial Velocity (RVL) algorithm definition (Tech. Rep.)*. ESA.

ESA. (2016). Sentinel-1 product definition, document S1-RS-MDA-52-7440. Retrieved from https://sentinel.esa.int/documents/247904/1877131/Sentinel-1-Product-Definition.pdf

ESA. (2022). *Report for mission selection: Earth explorer 10 candidate mission harmony*. European Space Agency.

Feistel, R., Nausch, G., & Wasmund, N. (2008). *State and evolution of the Baltic Sea, 1952–2005: A detailed 50-year survey of meteorology and climate, physics, chemistry, biology, and marine environment* (1st ed.), Wiley.

Fennel, W., & Sturm, M. (1992). Dynamics of the Western Baltic. *Journal of Marine Systems*, *3*(1), 183–205. https://doi.org/10.1016/0924-7963(92)90038-A

Gustafsson, B. (1997). Interaction between Baltic Sea and North Sea. *Deutsche Hydrographische Zeitschrift*, *49*(2–3), 165–183. https://doi.org/10.1007/BF02764031

Hajduch, G., Vincent, P., Cordier, K., Grignoux, M., Husson, R., Peureux, C., & Benchaabane, A. (2022). *S-1 annual performance report for 2022 (Tech. Rep.)*. ESA.

Hansen, M. W., Collard, F., Dagestad, K. F., Johannessen, J. A., Fabry, P., & Chapron, B. (2011). Retrieval of sea surface range velocities from Envisat ASAR Doppler centroid measurements. *IEEE Transactions on Geoscience and Remote Sensing*, *49*(10), 3582–3592. https://doi.org/10.1109/TGRS.2011.2153864

Hersbach, H., Bell, B., Berrisford, P., Biavati, H. A. G., Muñoz Sabater, J., Nicolas, J., et al. (2018). ERA5 hourly data on single levels from 1940 to present [Dataset]. *Copernicus Climate Change Service (C3S) Climate Data Store (CDS)*. https://doi.org/10.24381/cds.adbb2d47

Hersbach, H., Bell, B., Berrisford, P., Hirahara, S., Horányi, A., Muñoz-Sabater, J., et al. (2020). The ERA5 global reanalysis. *Quarterly Journal of the Royal Meteorological Society*, *146*(730), 1999–2049. https://doi.org/10.1002/qj.3803

Isern-Fontanet, J., Chapron, B., Lapeyre, G., & Klein, P. (2006). Potential use of microwave sea surface temperatures for the estimation of ocean currents. *Geophysical Research Letters*, *33*(24), L24608. https://doi.org/10.1029/2006GL027801

Jakobsen, F., Hansen, I. S., Ottesen Hansen, N.-E., & Østrup Rasmussen, F. (2010). Flow resistance in the great belt, the biggest strait between the North Sea and the Baltic Sea. *Estuarine, Coastal and Shelf Science*, *87*(2), 325–332. https://doi.org/10.1016/j.ecss.2010.01.014

Jakobsen, F., & Trébuchet, C. (2000). Observations of the transport through the belt sea and an investigation of the momentum balance. *Continental Shelf Research*, *20*(3), 293–311. https://doi.org/10.1016/S0278-4343(99)00073-4

Johannessen, J. A., Chapron, B., Collard, F., Kudryavtsev, V., Mouche, A., Akimov, D., & Dagestad, K. (2008). Direct ocean surface velocity measurements from space: Improved quantitative interpretation of Envisat ASAR observations. *Geophysical Research Letters*, *35*(22), L22608. https://doi.org/10.1029/2008GL035709

Krieger, G., Moreira, A., Fiedler, H., Hajnsek, I., Werner, M., Younis, M., & Zink, M. (2007). TanDEM-X: A satellite formation for high-resolution SAR interferometry. *IEEE Transactions on Geoscience and Remote Sensing*, *45*(11), 3317–3341. https://doi.org/10.1109/TGRS.2007.900693

Lass, H.-U., & Matthäus, W. (2008). General oceanography of the Baltic Sea. In *State and evolution of the Baltic Sea, 1952–2005* (pp. 5–43). John Wiley & Sons, Ltd. https://doi.org/10.1002/9780470283134.ch2

Li, C. (2022). *Time series data analysis in oceanography: Applications using MATLAB*. Cambridge University Press. https://doi.org/10.1017/9781108697101

Lindenthal, A., Nord, A., Ljungemyr, P., & Fyrstedt, S. (2023). *Baltic Sea physics analysis and forecast (Tech. Rep.)*. Copernicus marine service. https://doi.org/10.48670/moi-00010

Martin, A. C., Gommenginger, C. P., Jacob, B., & Staneva, J. (2022). First multi-year assessment of Sentinel-1 radial velocity products using HF radar currents in a coastal environment. *Remote Sensing of Environment*, *268*, 112758. https://doi.org/10.1016/j.rse.2021.112758

Martin, A. C., Gommenginger, C. P., & Quilfen, Y. (2018). Simultaneous ocean surface current and wind vectors retrieval with squinted SAR interferometry: Geophysical inversion and performance assessment. *Remote Sensing of Environment*, *216*, 798–808. https://doi.org/10.1016/j.rse.2018.06.013

Martin, A. C. H., Gommenginger, C., Marquez, J., Doody, S., Navarro, V., & Buck, C. (2016). Wind-wave-induced velocity in ATI SAR ocean surface currents: First experimental evidence from an airborne campaign. *Journal of Geophysical Research: Oceans*, *121*(3), 1640–1653. https://doi.org/10.1002/2015JC011459

Mattsson, J. (1996). Some comments on the Barotropic flow through the Danish straits and the division of the flow between the belt sea and the Öresund. *Tellus*, *48*(3), 456–464. https://doi.org/10.1034/j.1600-0870.1996.t01-2-00007.x

Moiseev, A., Johannessen, J. A., & Johnsen, H. (2022). Towards retrieving reliable ocean surface currents in the coastal zone from the Sentinel-1 Doppler shift observations. *Journal of Geophysical Research: Oceans*, *127*(5), e2021JC018201. https://doi.org/10.1029/2021JC018201

Moiseev, A., Johnsen, H., Johannessen, J. A., Collard, F., & Guitton, G. (2020). On removal of sea state contribution to Sentinel-1 Doppler shift for retrieving reliable ocean surface current. *Journal of Geophysical Research: Oceans*, *125*(9), e2020JC016288. https://doi.org/10.1029/2020JC016288

Morrow, R., Fu, L.-L., Ardhuin, F., Benkiran, M., Chapron, B., Cosme, E., et al. (2019). Global observations of fine-scale ocean surface topography with the Surface Water and Ocean Topography (SWOT) mission. *Frontiers in Marine Science*, *6*, 232. https://doi.org/10.3389/fmars.2019.00232

Mouche, A. A., Collard, F., Chapron, B., Dagestad, K.-F., Guitton, G., Johannessen, J. A., et al. (2012). On the use of Doppler shift for sea surface wind retrieval from SAR. *IEEE Transactions on Geoscience and Remote Sensing*, *50*(7), 2901–2909. https://doi.org/10.1109/TGRS.2011.2174998

Omstedt, A., Elken, J., Lehmann, A., Leppäranta, M., Meier, H., Myrberg, K., & Rutgersson, A. (2014). Progress in physical oceanography of the Baltic Sea during the 2003–2014 period. *Progress in Oceanography*, *128*, 139–171. https://doi.org/10.1016/j.pocean.2014.08.010

Rodríguez, E., Bourassa, M., Chelton, D., Farrar, J. T., Long, D., Perkovic-Martin, D., & Samelson, R. (2019). The winds and currents mission concept. *Frontiers in Marine Science*, *6*, 438. https://doi.org/10.3389/fmars.2019.00438

Romeiser, R., Breit, H., Eineder, M., Runge, H., Flament, P., de Jong, K., & Vogelzang, J. (2005). Current measurements by SAR along-track interferometry from a space shuttle. *IEEE Transactions on Geoscience and Remote Sensing*, *43*(10), 2315–2324. https://doi.org/10.1109/TGRS.2005.856116

TAC, C. M. I. S. (Ed.) (2023). *Product user manual for in situ products insitu_glo_phybgcwav_discrete_mynrt_013_030, insitu_arc_phybgcwav_discrete_mynrt_013_031, insitu_bal_phybgcwav_discrete_mynrt_013_032, insitu_ibi_phybgcwav_discrete_mynrt_013_033, insitu_blk_phybgcwav_discrete_mynrt_013_034, insitu_med_phybgcwav_discrete_mynrt_013_035, insitu_nws_phybgcwav_discrete_mynrt_013_036 (Report)*. https://doi.org/10.13155/43494

Thompson, D. R. (1989). Calculation of microwave Doppler spectra from the ocean surface with a time-dependent composite model. In G. J. Komen & W. A. Oost (Eds.), *Radar scattering from modulated wind waves: Proceedings of the workshop on modulation of short wind waves in the gravity-capillary range by non-uniform currents, held in Bergen Aan Zee, The Netherlands, 24–26 may 1988* (pp. 27–40). Springer Netherlands. https://doi.org/10.1007/978-94-009-2309-6_3

Thomson, R. E., & Emery, W. J. (2014). Chapter 5—Time series analysis methods. In R. E. Thomson & W. J. Emery (Eds.), *Data analysis methods in physical oceanography* (3rd ed.), pp. 425–591. Elsevier. https://doi.org/10.1016/B978-0-12-387782-6.00005-3

Torres, H., Wineteer, A., Klein, P., Lee, T., Wang, J., Rodriguez, E., et al. (2023). Anticipated capabilities of the ODYSEA wind and current mission concept to estimate wind work at the air–sea interface. *Remote Sensing*, *15*(13), 3337. https://doi.org/10.3390/rs15133337

Wang, C., Tandeo, P., Mouche, A., Stopa, J. E., Gressani, V., Longepe, N., et al. (2019). Classification of the global Sentinel-1 SAR vignettes for ocean surface process studies. *Remote Sensing of Environment*, *234*, 111457. https://doi.org/10.1016/j.rse.2019.111457

Yurovskaya, M., Kudryavtsev, V., Chapron, B., & Collard, F. (2019). Ocean surface current retrieval from space: The Sentinel-2 multispectral capabilities. *Remote Sensing of Environment*, *234*, 111468. https://doi.org/10.1016/j.rse.2019.111468

Yurovsky, Y., Kudryavtsev, V., Grodsky, S., & Chapron, B. (2019). Sea surface Ka-Band Doppler measurements: Analysis and model development. *Remote Sensing*, *11*(7), 839. https://doi.org/10.3390/rs11070839